



Article

The Post-Failure Spatiotemporal Deformation of Certain Translational Landslides May Follow the Pre-Failure Pattern

Luyao Wang¹, Haijun Qiu^{1,2,*} , Wenqi Zhou¹, Yaru Zhu¹, Zijing Liu¹, Shuyue Ma¹, Dongdong Yang¹ and Bingzhe Tang¹

- ¹ Shaanxi Key Laboratory of Earth Surface and Environmental Carrying Capacity, College of Urban and Environmental Sciences, Northwest University, Xi'an 710127, China; luyao wang@stumail.nwu.edu.cn (L.W.); zhouwenqi@stumail.nwu.edu.cn (W.Z.); zhuyaru@stumail.nwu.edu.cn (Y.Z.); liuzijing@stumail.nwu.edu.cn (Z.L.); msynwu@stumail.nwu.edu.cn (S.M.); yangdongdong@stumail.nwu.edu.cn (D.Y.); tangbz121@nwu.edu.cn (B.T.)
- ² Insitute of Earth Surface System and Hazards, College of Urban and Environmental Sciences, Northwest University, Xi'an 710127, China
- * Correspondence: haijunqiu@nwu.edu.cn; Tel.: +86-139-9134-5616

Abstract: Investigating landslide deformation patterns in different evolution stages is important for understanding landslide movement. Translational landslides generally slide along a relatively straight surface of rupture. Whether the post-failure spatiotemporal deformation for certain translational landslides follows the pre-failure pattern remains untested. Here, the pre- and post-failure spatiotemporal deformations of the Simencun landslide along the Yellow River in 2018 were analyzed through multi-temporal remote sensing image analysis, Interferometric Synthetic Aperture Radar (InSAR) deformation monitoring and intensive field investigations. The results show that the pre- and post-failure spatial deformations both follow a retrogressive failure pattern. The long time series of the displacement before and after failure is characterized by obvious seasonal and periodic stage acceleration movements. Effective rainfall played an important role in the increase of the displacement acceleration, and the change in temperature might have accelerated the displacement. Finally, there is a possibility that the post-failure spatiotemporal deformation pattern of translational landslides does follow the pre-failure pattern when certain conditions are satisfied. The results are of great significance to improving our understanding of the spatiotemporal deformation pattern of landslides and to post-failure risk prevention and control.

Keywords: landslides; deformation pattern; landslide movement; pre- and post-failure; InSAR



Citation: Wang, L.; Qiu, H.; Zhou, W.; Zhu, Y.; Liu, Z.; Ma, S.; Yang, D.; Tang, B. The Post-Failure Spatiotemporal Deformation of Certain Translational Landslides May Follow the Pre-Failure Pattern. *Remote Sens.* **2022**, *14*, 2333. <https://doi.org/10.3390/rs14102333>

Academic Editor: Francesca Ardizzone

Received: 27 February 2022

Accepted: 9 May 2022

Published: 12 May 2022

Publisher's Note: MDPI stays neutral with regard to jurisdictional claims in published maps and institutional affiliations.



Copyright: © 2022 by the authors. Licensee MDPI, Basel, Switzerland. This article is an open access article distributed under the terms and conditions of the Creative Commons Attribution (CC BY) license (<https://creativecommons.org/licenses/by/4.0/>).

1. Introduction

Landslides are a common geological hazard worldwide, causing huge casualties and economic losses every year [1–4]. Gathering landslide deformation information plays an important role in landslide risk prevention and control [5,6]. It is well known that most landslides have different deformation characteristics in different evolution stages [7–9]. Therefore, it is necessary to study the deformation patterns of landslides in different stages to formulate corresponding prevention strategies and reduce the risks landslides pose [10].

In recent years, many studies have been carried out on the deformation patterns of landslides. Some scholars made use of Deep Learning (DL) approaches, especially using Convolutional Neural Network (CNN) and Fully Convolutional Network (FCN) algorithms to conduct automatic landslide detection and obtain landslide spatial information [11–14]. The DL approaches show great advantages in landslide deformation prediction, but they cannot realize real-time monitoring of landslides [15]. Traditional landslide deformation detection methods, such as the Global Positioning System (GPS) and leveling techniques [16,17], can obtain landslide surface deformation information, but it is difficult to meet the needs of landslide monitoring because of the limited equipment.

With the development of the Remote Sensing (RS) technology, unmanned aerial system (UAS) photogrammetry [18–21], light detection and ranging (LiDAR) [22–25], terrestrial laser scanning (TLS) [26,27] and other advanced measurements, technology is gradually applied in the field of landslides. By using these remote sensing techniques, the deformation process can be detected in real-time, and the changes in topographic features can be quantitatively analyzed [28]. Although these methods have high accuracy, they are difficult to be widely applied to the analysis of landslides due to their high cost and low efficiency. The Interferometric Synthetic Aperture Radar (InSAR) is characterized by being all-weather, low cost and having convenient operation [29–31]. A variety of time-series InSAR approaches were developed by different researchers, for example, the Small Baseline Subset Approach (SBAS) [32,33], the Permanent Scatterer InSAR (PS-InSAR) [34,35] and pixel offset tracking (POT) [36]. It can trace landslide displacement and monitor deformation processes in real-time with centimeter to millimeter-scale accuracy; InSAR has gradually been widely used in the study of landslide deformation [37,38].

Because translational landslides are the most common type of landslide that causes catastrophic damage around the world [39,40], it is important to study their deformation pattern changes for building corresponding prevention and control projects. Detecting the deformations of landslides by using InSAR has attracted the attention of many scholars. Some scholars have studied regional stability by detecting the deformations of potential landslides in large regions [41–44]. Several scholars traced the pre-failure deformation process of landslides and studied the evolution characteristics and trigger factors [45–48]. Several studies analyzed the landslide movement trend and gave risk warnings by monitoring the long time-series displacement before and after the landslide occurred [49–52]. However, few early studies have directly focused on whether the deformation patterns change after landslide failure. Li et al. [53] and Zhu et al. [54] found that there were different failure patterns of retrogression and advancing progress before and after the failure of the Huangnibazi and Jianguo landslides. In contrast, Zhao et al. [55] found that the Xinyuan No. 2 landslide repeatedly exhibited retrogressive failure within the same landslide body. However, the continuity of the post-failure deformation pattern has not been determined. Under what circumstances the post-failure deformation follows the pre-failure deformation is still a question that needs to be studied.

Therefore, the main objective of this study was to determine whether the pre- and post-failure deformation patterns of certain translational landslides are consistent. First, we retrieved the pre- and post-failure spatiotemporal deformation process through InSAR deformation monitoring. Then, the pre- and post-failure spatial movement trends were compared. In addition, the long time-series displacement data of the landslide were extracted and were comprehensively analyzed, along with the effective antecedent rainfall and temperature. The results of this study are of great significance for improving our understanding of the spatiotemporal deformation patterns of landslides and for conducting corresponding post-failure prevention and control work.

2. Study Area

The study area is located in Kangyang Town, Jianzha County, Qinghai Province (Figure 1a), in the transition zone between the strongly uplifted Tibetan Plateau and the relatively less uplifted Loess Plateau. This region is characterized by active regional tectonic movement and poor stratigraphic stability. Various landforms, such as valleys, hills and mountains, are widely developed, and the vertical difference in the terrain is significant. The Yellow River flows through this area from northwest to southeast (Figure 1b), and it has an erosion and cutting effect on the front edge of the slope, providing favorable topographic and geomorphological conditions for landslide development. The average annual temperature in this area is 7.8 °C. The average annual precipitation is 350–500 mm, which is mostly concentrated in summer and autumn [56]. Therefore, owing to the climatic conditions, landforms and other factors, landslides are widespread in this area, and the

large, extra-large and giant landslides are typical and representative of those around the world [57,58].

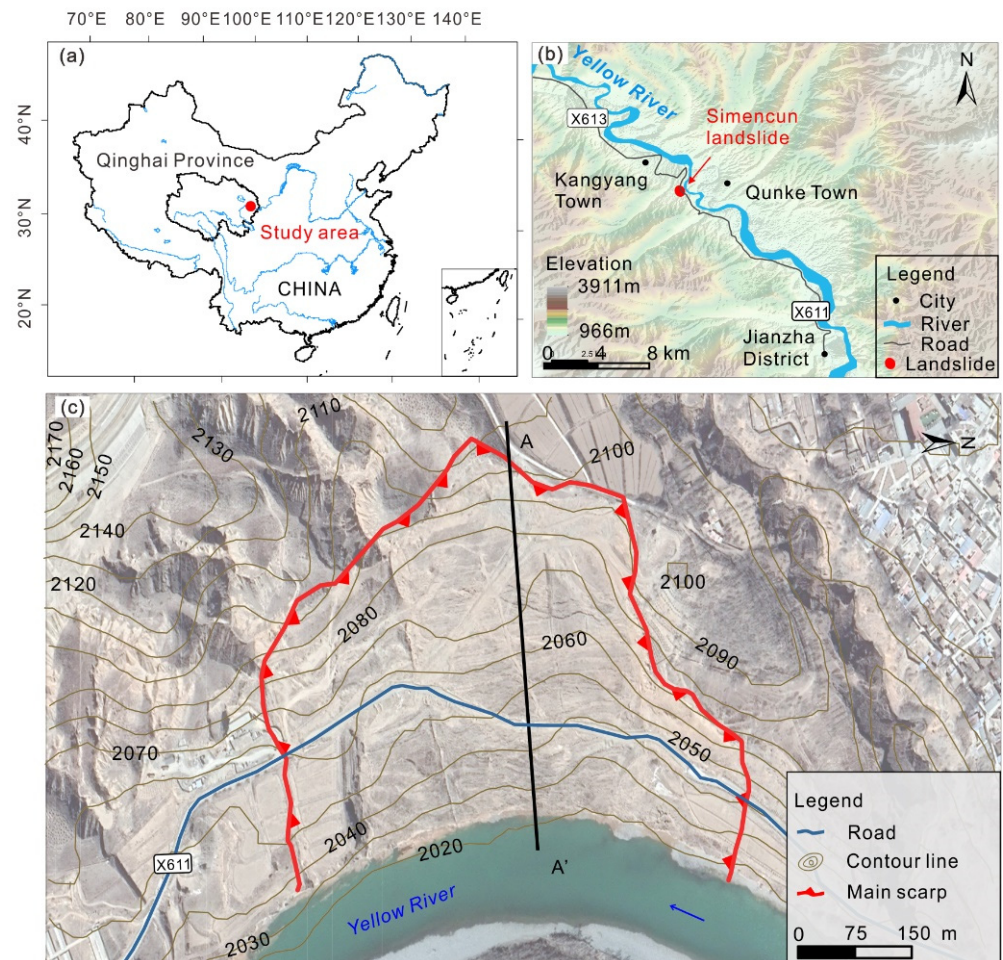


Figure 1. (a,b) Location of the Simencun landslide. (c) Geomorphological features of the Simencun landslide.

On 3 April 2018, the Simencun Landslide in Qinghai Province began to slip. By 18:00 on 4 April 2018, the minor scarp had become temporarily stable, and the landslide had slid down 5 to 10 m, making it a typical translational landslide. The landslide was composed of Quaternary alluvial loess-like soil (Q_4^{dl-pl}) and Neogene mudstone (N) (Figure 2). The slope direction was 100° , and the main sliding direction was the same as the slope direction [59]. The height of the main scarp was about 8 to 25 m (Figure 3b). The main body was about 390 m long and 500 m wide. The landslide severely damaged the Makang highway (Figure 3c,e), power transmission lines (Figure 3b), drainage channels (Figure 3d) and other public facilities, causing huge social and economic losses.

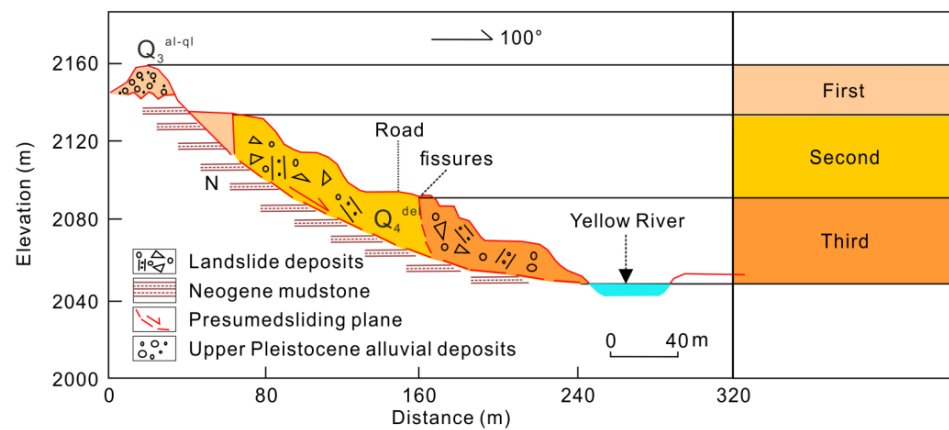


Figure 2. Longitudinal profile of the Simencun landslide (modified from Shi et al. [59]). A–A' in Figure 1c is the Longitudinal section position.

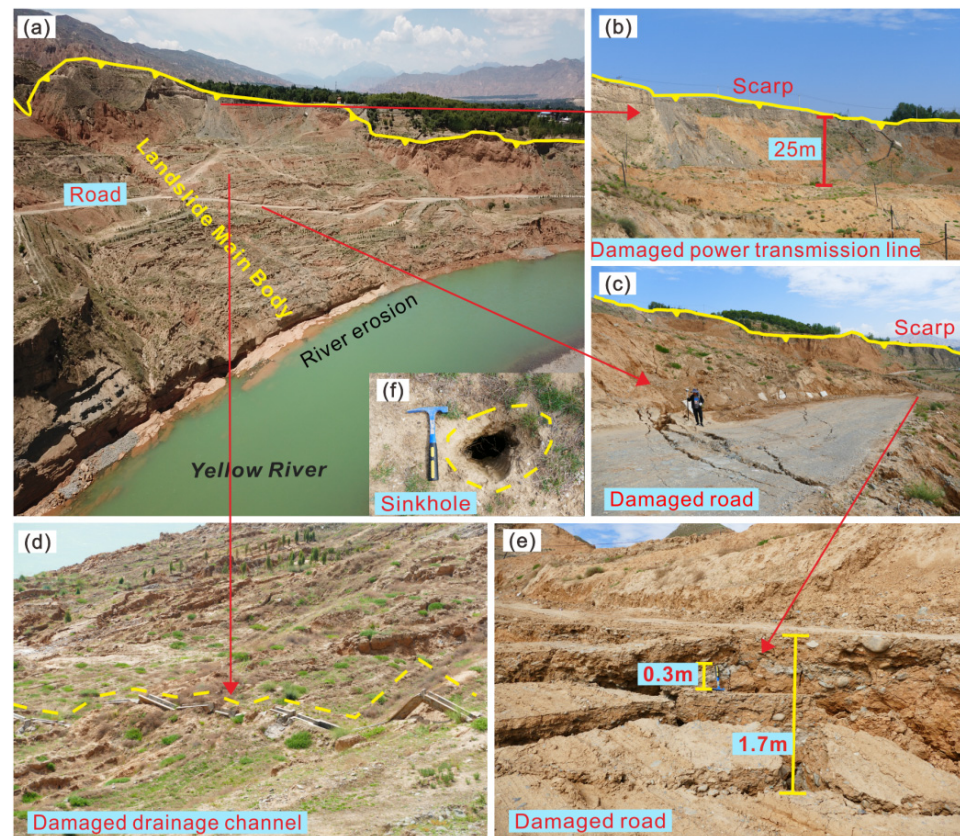


Figure 3. Field investigation of the Simencun landslide: (a) Landslide's main body, (b–e) damaged public facilities and (f) sinkhole.

3. Materials and Methodology

3.1. Time-Series InSAR Analysis

Interferometric Point Target Analysis (IPTA) was used in this study, which was developed based on Persistent Scatterer Interferometry (PSI) [60,61]. First of all, the obtained image formed the image interference pair of time series by differential interferometry. Second, the points that had low spectral diversity [61] and low amplitude dispersion [35] were selected for analysis. Third, based on the two-dimensional (2D) linear regression pattern, differential interference calculation, adaptive filtering and phase unwrapping were carried out on these points through iterative regression analysis. We removed the orbital error, topographic phase, atmospheric phase, and then refined the unwrapped phase. Then

the Singular Value Decomposition (SVD) method [62] was used to extract the linear time series displacement. After separating the linear deformation, the residual phase could be expressed by the following equation:

$$\varphi_i^{res} = \varphi_i^{nl} + \varphi_i^a + \varphi_i^n \quad (1)$$

where φ_i^{res} is residual phase, φ_i^{nl} is nonlinear deformation phase, φ_i^a is atmospheric delay phase and φ_i^n is phase noise. Because the nonlinear deformation and atmospheric delay phase were spatially manifested as low-frequency characteristics, the noise was manifested as a high-frequency phase. Therefore, low pass filtering was carried out to remove interferometric decorrelation and other noise components, and then high pass filtering was carried out to obtain nonlinear deformation. Finally, the true deformation phase was obtained by adding linear deformation and nonlinear deformation.

In this study, we used GAMMA synthetic aperture radar interferometry software, which is a fully functional data platform developed by GAMMA Remote Sensing AG in Switzerland for interferometric radar data processing. Since the pre- and post-failure surface displacement changed dramatically, spatial and temporal decorrelation of the radar SAR images occurs [63,64]. Serious decorrelation affects the quality of the interference results, making it difficult to extract accurate deformation information. Separately monitoring the pre- and post-failure can greatly improve the accuracy of the measurement results. Thereby taking the time at which the landslide occurred as the node, two sets of pre-failure (from 7 January 2017 to 27 March 2018) and post-failure (from 8 April 2018 to 28 April 2021) Sentinel-1 datasets were processed and analyzed, and 117 and 264 interferometric pairs were generated, respectively (Figure 4). In addition, we selected coherent targets with a coherence of greater than 0.5 as the PS points for the subsequent deformation processing. POD Precise Orbit Ephemerides were used to remove orbit error, and Shuttle Radar Topography Mission (SRTM) digital elevation model (DEM) data covering the study area with a resolution of 30 m was used as the reference elevation data to eliminate the topographic phase.

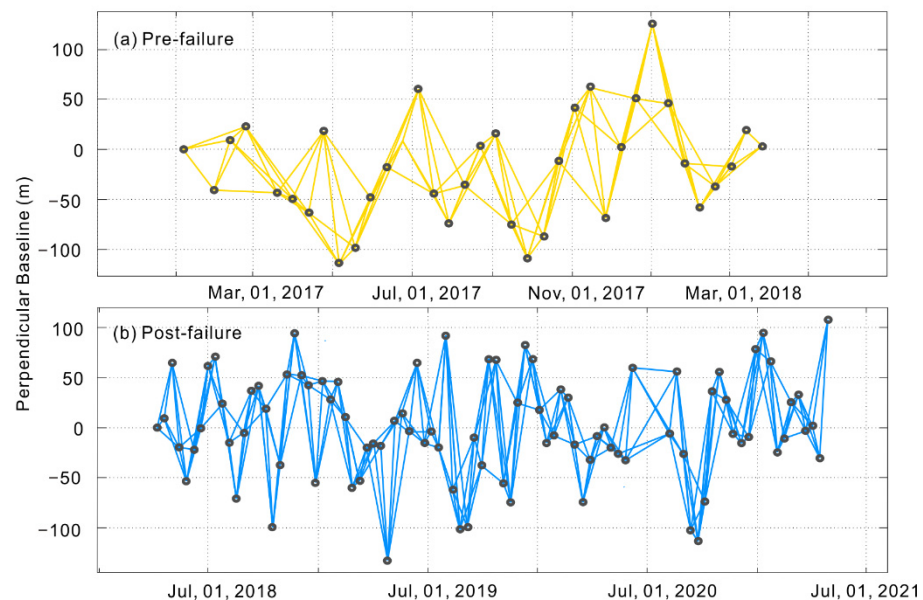


Figure 4. Spatial and temporal baselines of the Sentinel-1 data used in this study: (a) pre-failure spatial and temporal baselines, (b) post-failure spatial and temporal baselines.

3.2. Effective Antecedent Rainfall

The amount of water that actually seeps into a hillside during the rainfall before the landslide occurs is defined as the effective antecedent rainfall [65]. The effective antecedent rainfall reduces the stability of the soil and is an important factor inducing the

landslide [66,67]. The influence of the rainfall on the slope during a period of time before a certain day is an attenuation process, and the influence of the rainfall on the soil moisture during the previous n days is related to the precipitation during the previous $(n - 1)$ days. Thus, in this study, the effective antecedent daily rainfall was calculated using the following weighted summation equation [68,69]:

$$P_b = \sum_1^n P_i \cdot K_i \quad (2)$$

where P_b is the effective antecedent rainfall, P_i is the daily rainfall on the i -th day preceding the landslide event ($1 \leq i \leq n$) and K_i is the decay coefficient due to evaporation. Here, following [70], K_i was set to 0.84, and n was set to 10.

4. Results and Analysis

4.1. Basic Displacement Characteristics of the Landslide

Through visual interpretation of multi-temporal optical remote sensing images, the vector data for the landslide's surface displacement can be extracted [71]. We obtained the Planet satellite's high-resolution remote sensing images of the pre-failure (3 June 2016) and post-failure (1 December 2018) conditions in the study area, with a resolution of 0.5 m. The pre- and post-failure visible ground objects and characteristic points were vectorized (Figure 5). It was found that the landslide was greatly deformed and slid downward, causing serious damage to a road. The middle and lower parts were the most seriously deformed areas, with an average displacement of about 30 m, which was mainly caused by river erosion. Moreover, the cross-section of the Yellow River at the foot of the Simencun landslide (about 1/2 or 1/3 of the normal width) was significantly smaller than upstream and downstream (Figures 1b and 3a). Such a bottleneck shape was prone to rapids and thus aggravated the erosion intensity of the lateral impact [72].

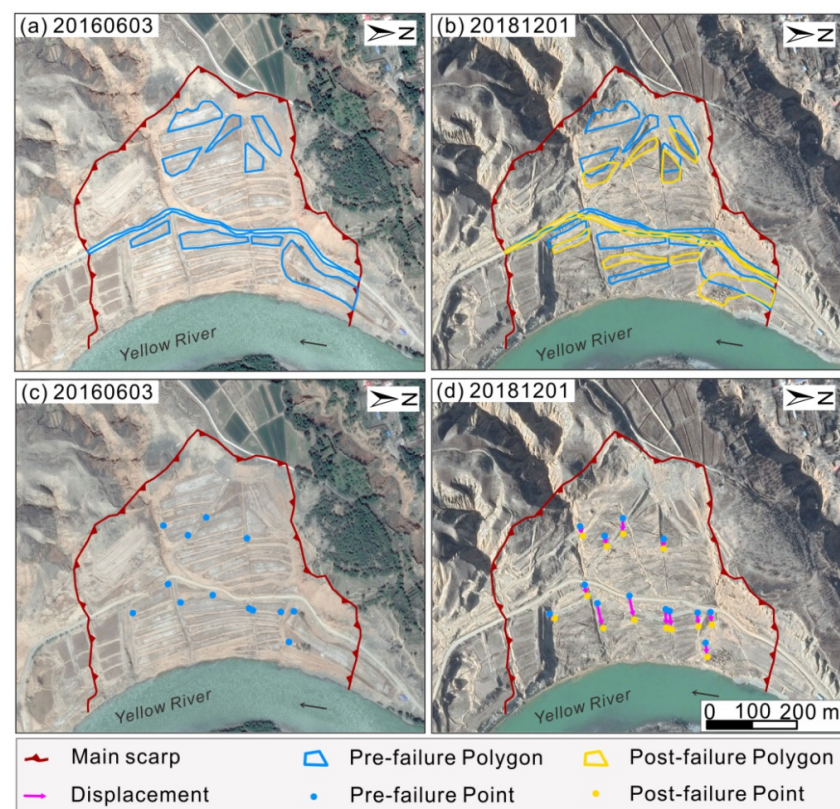


Figure 5. Surface travel distance of Simencun landslide: (a,b) ground objects, (c,d) feature points.

In the direction perpendicular to the sliding direction, the displacement of the northern side was stronger than that of the southern side, and a large area of the north side of the toe collapsed (Figure 5). This is consistent with the field investigation results. The different deformation degrees on the north and south sides could be caused by the differences in the intensity of the river erosion. The northern edge of the landslide has a more convex shape and is located upstream of the river (Figure 1b), which may be the reason for the more intense deformation of the north side [73].

4.2. Spatial Deformation Pattern of the Simencun Landslide

4.2.1. Pre-Failure Spatial Deformation

Figure 6 shows the pre- and post-failure mean Line of Sight (LOS) deformation velocity, negative values indicate movement away from the satellite, and positive values represent movement toward the satellite. The deformation velocity was not uniform in the interior part of the landslide. The middle and lower parts had the largest deformation velocities, and the maximum LOS deformation velocity was up to -124 mm/a.

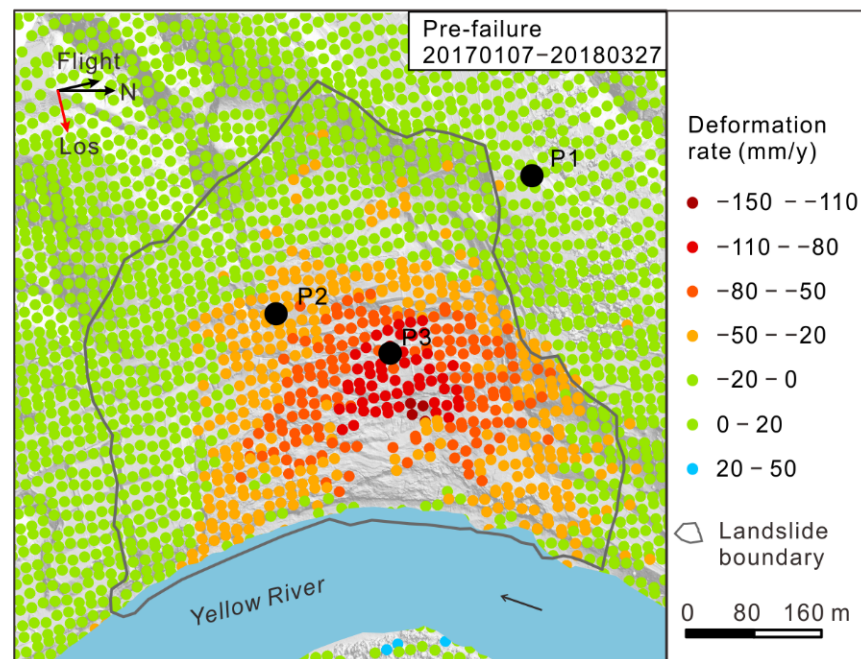


Figure 6. Pre-failure mean LOS deformation velocity.

To further research the spatial deformation of the landslide, we studied the pre-failure cumulative LOS displacement (Figure 7). The lower part became unstable the earliest, which is mainly attributed to the river eroding away the weak structural plane at the bottom of the slope (Figure 3a). Then, because the original balance of the structure of the lower part was destroyed, the upper part lost its support, and the deformation area gradually extended into the upper and surrounding areas. By 27 March 2018, the maximum cumulative LOS displacement deformation reached -135 mm, and the evolution exhibited a typical retrogressive failure pattern.

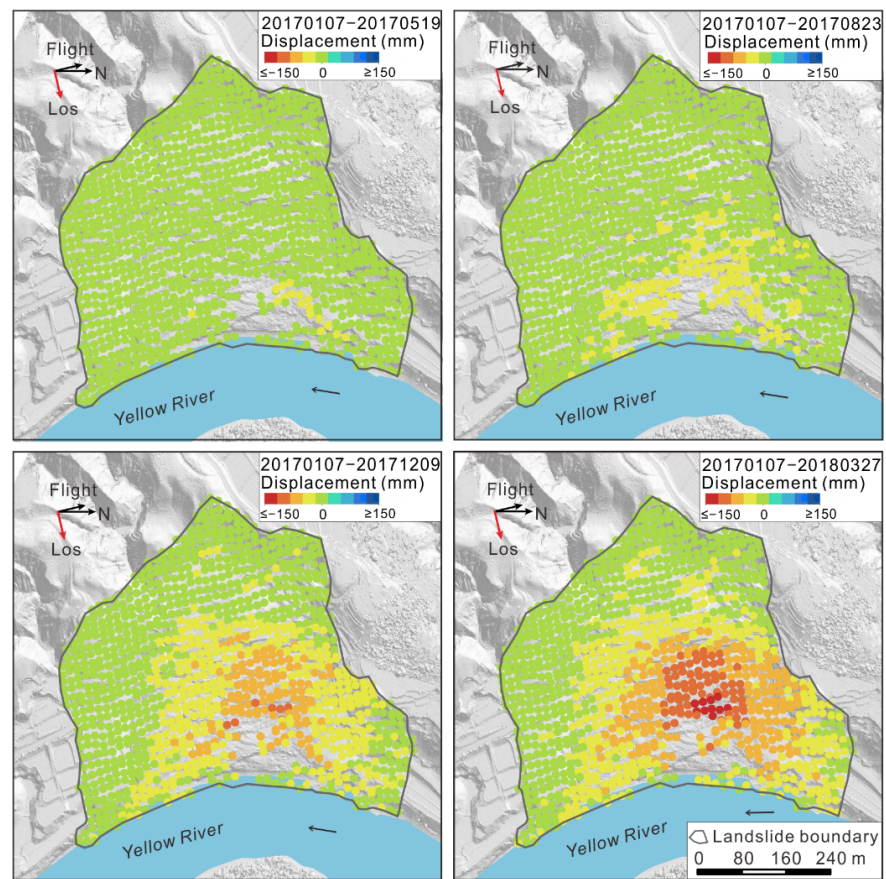


Figure 7. Pre-failure cumulative LOS displacement.

4.2.2. Post-Failure Spatial Deformation

The toe was continuously eroded by the river, and no obvious accumulation was produced at the front edge after the landslide occurred. In Figure 8, the mean LOS deformation velocity was relatively small, only 1/3 that of the pre-failure value, but the area with the largest deformation velocity after the landslide occurred was still located in the lower part of the main body.

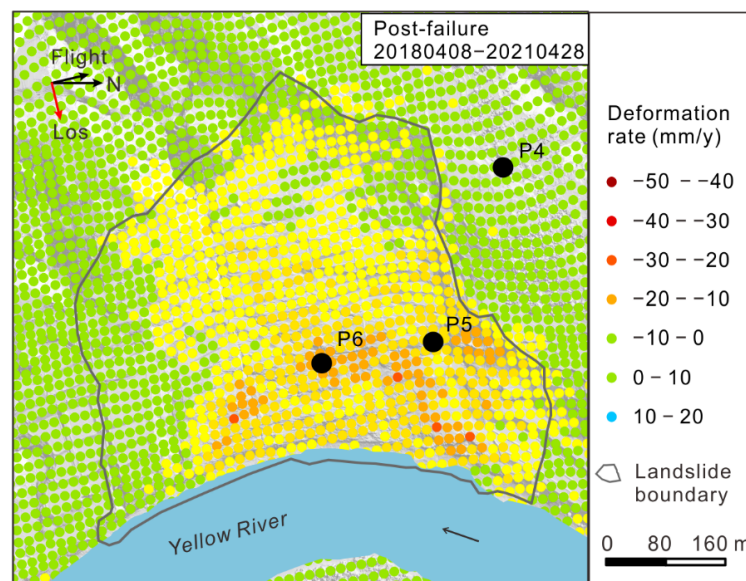


Figure 8. Post-failure mean LOS deformation velocity.

Furthermore, the post-failure cumulative LOS displacement was divided at the same scale as the pre-failure displacement (Figure 9). There was still a deformation trend extending from the middle and lower parts to the surrounding area after the landslide occurred. The deformation area extended to the entire landslide, and the overall deformation of the landslide was apparent. Until 28 April 2021, the landslide was still deforming, with a maximum cumulative LOS displacement of -145 mm. In conclusion, after the occurrence of the Simencun landslide, it was still in an unstable state, the post-failure spatial deformation pattern followed the pre-failure retrogressive failure pattern, and the deformation trend of extending from the middle and bottom into the surrounding area was maintained.

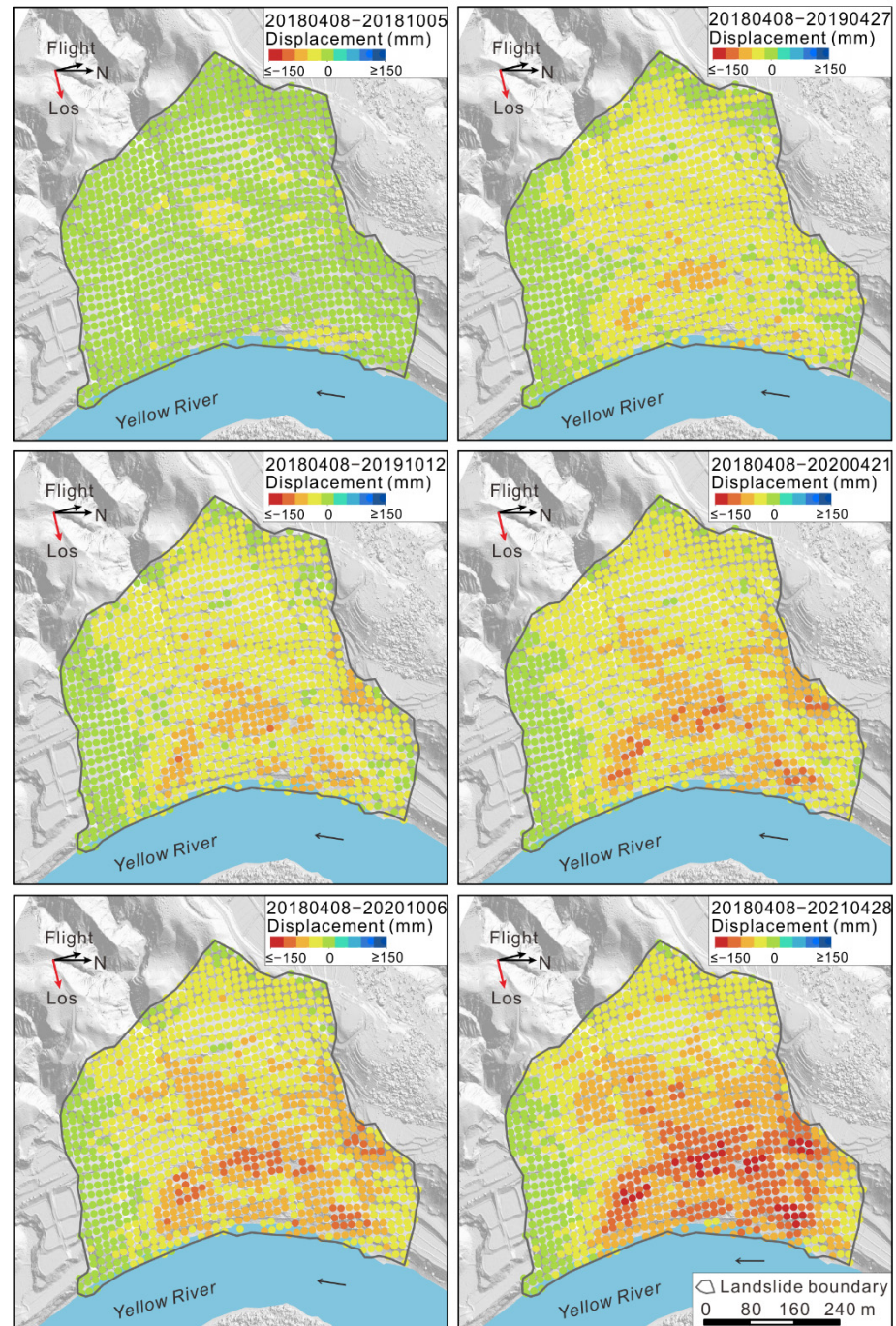


Figure 9. Post-failure cumulative LOS displacement.

4.3. Time-Series of Landslide Displacement

4.3.1. Acceleration of Displacement before Failure

The temporal variation of displacement was complex. To explore the temporal evolution of the Simencun landslide, the time series LOS displacement at representative points in areas with different deformation velocities were calculated (Figure 10). The deformation before the rainfall was gentle but accelerated in the late period of seasonal rainfall. From January to August 2017, the main body was still in a relatively stable state and moved slowly at certain acceleration, with a cumulative LOS displacement of about -23 mm. In August 2017, in the later period of the seasonal rainfall, the continuous rainfall reduced the stability of the landslide and changed the acceleration of the time series LOS displacement. In addition, the deformation velocity began to increase. Furthermore, after the rainy season, the landslide continued to accelerate during the winter. By March 2018, the cumulative LOS displacement of point P3, which was located in the most active area, had reached -97 mm. In conclusion, according to the InSAR deformation monitoring results, the pre-failure displacement deformation of the Simencun landslide experienced an accelerated movement stage in the late period of seasonal rainfall.

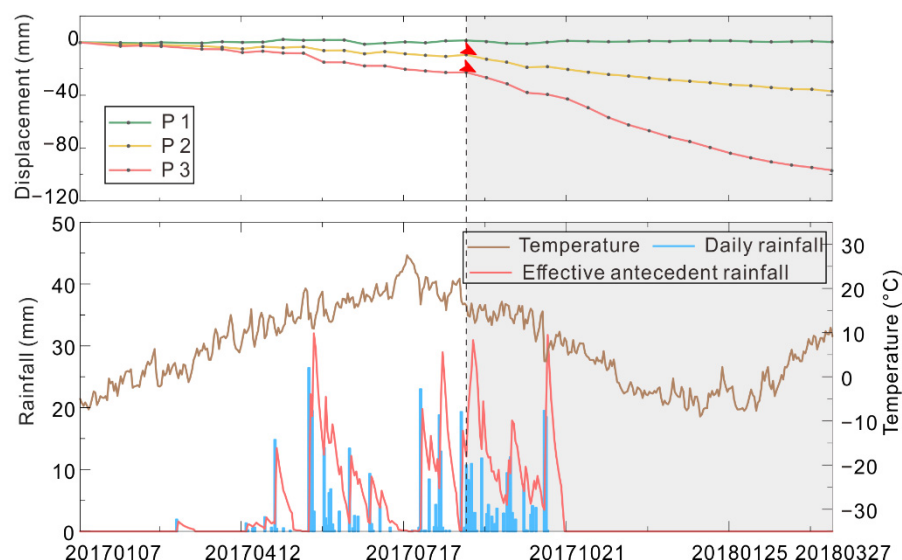


Figure 10. The time-series LOS displacement, effective antecedent rainfall and temperature before the landslide occurred. The locations of P1, P2 and P3 are shown in Figure 6. The red triangle represents the beginning of the accelerated change. The gray bar represents the time span of the accelerated displacement.

4.3.2. Seasonal Acceleration of Displacement after Failure

We can further understand the movement of landslides in different stages through continuous monitoring. From April 2018 to April 2021, there were three acceleration changes in the displacement of the Simencun landslide, which all occurred in the late rainy season and winter (Figure 11). The time spans and cumulative LOS displacements of the three accelerated deformation periods were as follows: from 23 September 2018 to 22 March 2019 (from -12.8 to -54.1 mm); from 18 September 2019 to 4 March 2020 (from -60.5 to -75.5 mm); and from 31 August 2020 to 4 April 2021 (from -77.1 to -106.2 mm). The acceleration of the displacement changed, and the deformation rate began to increase when seasonal rainfall acted on the landslide, reaching a certain threshold. More importantly, every winter and spring, the displacement still exhibited an obvious proportional relationship with the change in temperature, so it is considered to be affected by seasonal freezing and thawing. Therefore, it was determined that the post-failure displacement experienced the same accelerated deformation stage in the late period of

seasonal rainfall as the pre-failure displacement, and the accelerated deformation period exhibited seasonality.

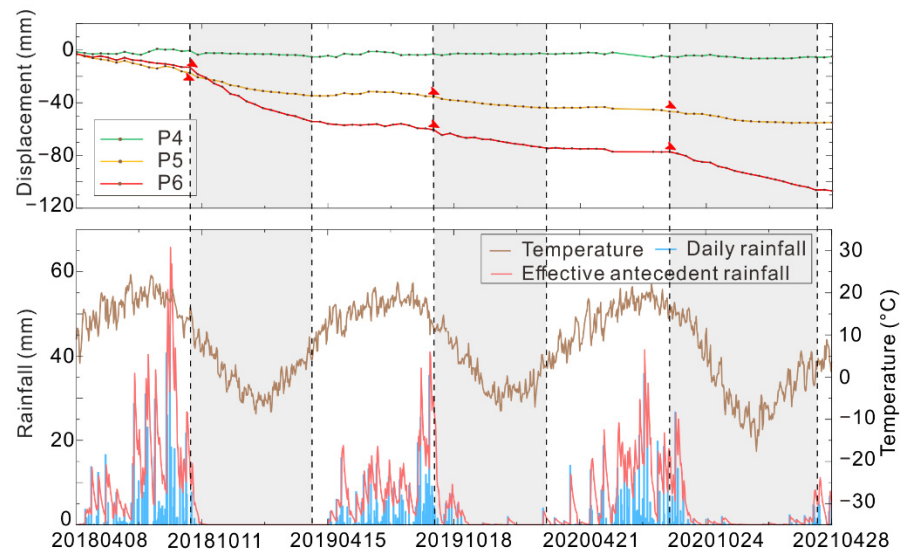


Figure 11. The time-series LOS displacement, effective antecedent rainfall and temperature after the landslide occurred. The locations of P4, P5 and P6 are shown in Figure 8. The red triangle represents the beginning of the accelerated change. The gray bar represents the time span of the accelerated displacement.

5. Discussion

5.1. Periodic Acceleration of Landslides

To further illustrate the periodic acceleration of landslides, we removed the linear component from the time-series cumulative LOS displacement obtained from the original InSAR monitoring and compared the de-linearized InSAR measurements with the effective antecedent rainfall and temperature data (Figure 12). The results demonstrate that the time-series deformation evidently had seasonal variability and was most active in the late rainy season and in winter and spring. The deformation had a period of one year on the inter-annual, and it was highly correlated with the local climate and was similar to the results of previous studies [74,75].

We confirmed that the effective antecedent precipitation played an important role in controlling the change in the acceleration of the Simencun landslide displacement. In Figures 10 and 11, there was no rainstorm ($25 \text{ mm} < \text{precipitation} < 50 \text{ mm}$ within 24 h) in seven days before the accelerated change, indicating that the accelerated change was not caused by a rainstorm. The changes in the acceleration of displacement occurred in August or September, which was late in the rainy season, and usually about 1 month after the peak in the effective antecedent rainfall (Figure 12, red arrows). This demonstrates that the continuous precipitation infiltration increased the soil moisture content and reduced the shear strength of soil and slope stability. After reaching a certain threshold, the landslide displacement velocity increased [76]. Therefore, it can be determined that the increase in displacement acceleration was caused by the effective antecedent rainfall.

Moreover, the period of severe displacement deformation was mostly concentrated in autumn and winter (Figures 10 and 11). With the decrease in temperature, the landslide displacement gradually accelerated, and the interval between the minimum temperature and the midpoint of the accelerated deformation period was about 2 weeks (Figure 12, blue arrows). In addition, the study area is located in the seasonal frozen soil area on the eastern edge of the Tibetan Plateau, and thus, the slope may be subjected to seasonal freezing–thawing [77]. The cyclic process of freezing in winter and thawing in spring destroys the soil structure and weakens the physical parameters. Consequently, it is recommended that

the post-failure prevention and monitoring be strengthened in winter and spring to reduce the possibility of the landslide slipping again and minimize losses caused by landslides.

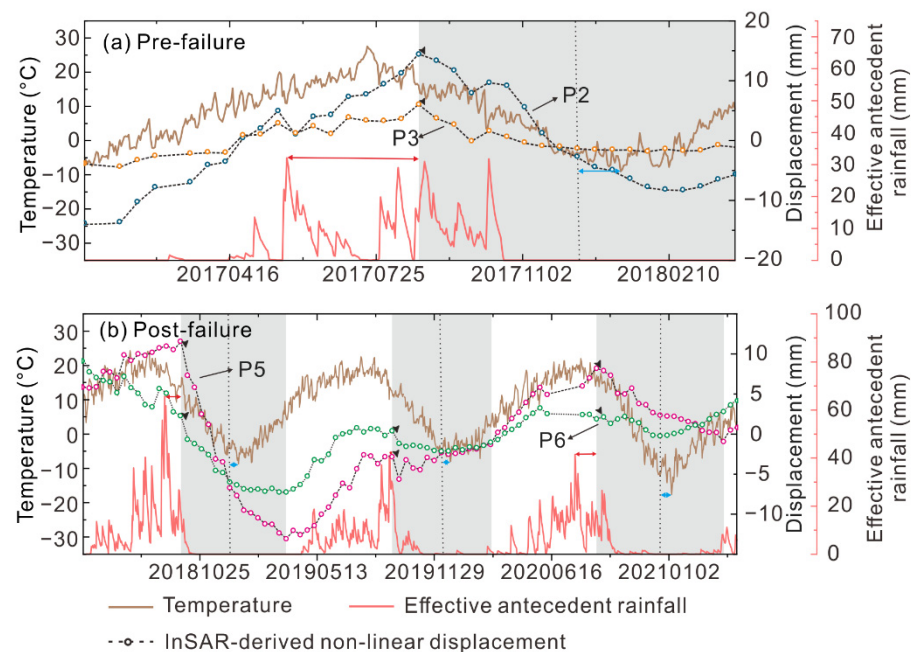


Figure 12. Time-series InSAR with linear trend removal, effective antecedent rainfall and temperature. The locations of P2 and P3 are shown in Figure 6. The locations of P5 and P6 are shown in Figure 8. The black triangles denote the initiation of the accelerated change. The gray bar represents the time span of the accelerated displacement. The red arrows represent the gap between the accelerated change and the peak in previous effective rainfall. The blue arrows represent the gap between the midpoint of the time span of the accelerated displacement and the lowest temperature value.

5.2. Continuity of Spatiotemporal Deformation Pattern

Addressing the deformation in different stages is significant for understanding the mechanism of landslide evolution and for disaster warnings [78–80]. In this study, we investigated the pre- and post-failure spatiotemporal deformation by monitoring the Simencun landslide for a long period of time. Before the landslide occurred, the lower part became unstable the earliest, and then the upper part lost support and began to slide, corresponding to a retrogressive failure pattern. After the landslide occurred, the deformation on the lower part was more intense than on the upper part. What is more, the post-failure spatial deformation still presented a retrogressive failure pattern. This was consistent with the behavior of the Aniangzhai (ANZ) landslides [81], which were influenced by rainfall and river erosion. The main reason was that there was no obvious accumulation changing the original movement environment due to river erosion after the landslide occurred. In addition, Zhao et al. [55] found that the xinyuan No. 2 landslide continued to slide forward in a regressive progressive deformation pattern because there was no obvious accumulation area in the lower part of the landslide. Jiao et al. [82] found that the landslide continued to slide along the original sliding direction because the sliding body was not blocked. On the contrary, the Jiangou landslide [54] shows different failure patterns of retrogression and advancing progressive before and after the failure. The main reason was that the Jiangou landslide had a formed dammed lake after the landslide occurred, the dammed lake constantly acted on the landslide, the stress environment of the landslide was changed again when the dammed lake collapsed, and its deformation pattern was changed. Therefore, the post-failure deformation of certain translational landslides will follow the pre-failure pattern if the original sliding and stress environment of landslides are not changed. It is meaningful for improving our understanding of translational landslide deformation and

conducting hazard prevention and control in advance in the areas and time periods in which collapse may occur.

6. Conclusions

The goal of this study was to determine whether the post-failure deformation of certain translational landslides follows the pre-failure pattern through long-term spatiotemporal deformation monitoring. Driven by river erosion, the spatial deformation of the Simencun landslide extended from the middle and lower parts to the surrounding area. The post-failure spatial deformation followed the pre-failure pattern and exhibited a retrogressive failure pattern on the landslide. In addition, the pre- and post-failure temporal displacements had similar stage acceleration. We confirmed that the landslide displacement was seasonal and periodic under the influence of climate, and the effective antecedent rainfall was the primary factor affecting the change in the acceleration of the displacement. Our results suggest that translational landslides will remain unstable after they occur, and the post-failure spatiotemporal deformation may follow the pre-failure pattern when the post-failure movement environment and the external forces remain almost unchanged. The results provide a new idea for studying the landslide movement patterns before and after a landslide has occurred and are helpful for elucidating the spatiotemporal evolution of translational landslides and reducing the risk of landslides. The results of this study suggest that there is a possibility for the continuation of the pre- and post-failure deformation pattern, but further research still needs to be done to prove this possibility.

Author Contributions: Conceptualization, H.Q.; methodology, L.W. and H.Q.; software, L.W., Y.Z. and Z.L.; validation, W.Z. and Y.Z.; formal analysis, L.W., W.Z. and Y.Z.; investigation, L.W., S.M., D.Y. and W.Z.; resources, H.Q.; data curation, L.W. and Y.Z.; writing—original draft preparation, L.W.; writing—review and editing, H.Q.; visualization, L.W., S.M. and B.T.; supervision, H.Q.; project administration, H.Q.; funding acquisition, H.Q. All authors have read and agreed to the published version of the manuscript.

Funding: This research was funded by the International Science and Technology Cooperation Program of China (Grant No. 2018YFE0100100), the Second Tibetan Plateau Scientific Expedition and Research Program (STEP) (Grant No. 2019QZKK0902) and the Natural Science Basic Research Program of Shaanxi (Grant No. 2021JC-40).

Institutional Review Board Statement: Not applicable.

Informed Consent Statement: Not applicable.

Data Availability Statement: The Sentinel-1A data used in this study were provided by the European Space Agency (ESA), <https://search.asf.alaska.edu/#/> (accessed on 12 April 2021); POD Precise Orbit Ephemerides used in this study were provided by the ESA, https://s1qc.asf.alaska.edu/aux_poeorb/ (accessed on 12 April 2021); and the SRTM DEM was freely downloaded from the website <https://earthexplorer.usgs.gov/> (accessed on 12 April 2021).

Acknowledgments: The authors thank the ESA for providing free Sentinel-1A datasets. The authors also thank the Google Earth Platform for providing the optical remote sensing images.

Conflicts of Interest: The authors declare no conflict of interest.

References

1. Petey, D.N. Global patterns of loss of life from landslides. *Geology* **2012**, *40*, 927–930. [[CrossRef](#)]
2. Froude, M.J.; Petley, D.N. Global fatal landslide occurrence from 2004 to 2016. *Nat. Hazard Earth Syst.* **2018**, *18*, 2161–2181. [[CrossRef](#)]
3. Qiu, H.; Cui, Y.; Pei, Y.; Yang, D.; Hu, S.; Wang, X.; Ma, S. Temporal patterns of nonseismically triggered landslides in Shaanxi Province, China. *CATENA* **2019**, *187*, 104356. [[CrossRef](#)]
4. Zhou, W.; Qiu, H.; Wang, L.; Pei, Y.; Tang, B.; Ma, S.; Yang, D.; Cao, M. Combining rainfall-induced shallow landslides and subsequent debris flows for hazard chain prediction. *CATENA* **2022**, *213*, 106199. [[CrossRef](#)]
5. Hervás, J.; I Barredo, J.; Rosin, P.L.; Pasuto, A.; Mantovani, F.; Silvano, S. Monitoring landslides from optical remotely sensed imagery: The case history of Tessina landslide, Italy. *Geomorphology* **2003**, *54*, 63–75. [[CrossRef](#)]

6. Schuster, R.L.; Highland, L.M. The Third Hans Cloos Lecture. Urban landslides: Socioeconomic impacts and overview of mitigative strategies. *Bull. Eng. Geol. Environ.* **2007**, *66*, 1–27. [[CrossRef](#)]
7. Cruden, D.M.; Varnes, D.J. Landslides: Investigation and mitigation. Chapter 3—Landslide types and processes. *Transp. Res. Board* **1996**, *247*, 36–75.
8. Delacourt, C.; Allemand, P.; Berthier, E.; Raucoules, D.; Casson, B.; Grandjean, P.; Pambrun, C.; Varel, E. Remote-sensing techniques for analysing landslide kinematics: A review. *Bull. Soc. Geol. Fr.* **2007**, *178*, 89–100. [[CrossRef](#)]
9. Eker, R.; Aydın, A. Long-term retrospective investigation of a large, deep-seated, and slow-moving landslide using InSAR time series, historical aerial photographs, and UAV data: The case of Devrek landslide (NW Turkey). *CATENA* **2020**, *196*, 104895. [[CrossRef](#)]
10. Zhang, Y.; Meng, X.; Jordan, C.; Novellino, A.; Dijkstra, T.; Chen, G. Investigating slow-moving landslides in the Zhouqu region of China using InSAR time series. *Landslides* **2018**, *15*, 1299–1315. [[CrossRef](#)]
11. Phuong, T.; Panahi, M.; Khosravi, K.; Ghorbanzadeh, O.; Kariminejad, N.; Cerda, A.; Lee, S. Evaluation of deep learning algorithms for national scale landslide susceptibility mapping of Iran. *Geosci. Front.* **2021**, *12*, 505–519.
12. Chen, Z.; Zhang, Y.; Ouyang, C.; Zhang, F.; Ma, J. Automated landslides detection for mountain cities using multi-temporal remote sensing imagery. *Sensors* **2018**, *18*, 821. [[CrossRef](#)] [[PubMed](#)]
13. Sameen, M.I.; Pradhan, B. Landslide Detection Using Residual Networks and the Fusion of Spectral and Topographic Information. *IEEE Access* **2019**, *7*, 114363–114373. [[CrossRef](#)]
14. Ghorbanzadeh, O.; Crivellari, A.; Ghamisi, P.; Shahabi, H.; Blaschke, T. A comprehensive transferability evaluation of U-Net and ResU-Net for landslide detection from Sentinel-2 data (case study areas from Taiwan, China, and Japan). *Sci. Rep.* **2021**, *11*, 14629. [[CrossRef](#)] [[PubMed](#)]
15. Yang, D.; Qiu, H.; Ma, S.; Liu, Z.; Du, C.; Zhu, Y.; Cao, M. Slow surface subsidence and its impact on shallow loess landslides in a coal mining area. *CATENA* **2021**, *209*, 105830. [[CrossRef](#)]
16. Marschalko, M.; Yilmaz, I.; Bednárík, M.; Kubecka, K. Influence of underground mining activities on the slope deformation genesis: Doubrava Vrchovec, Doubrava Ujala and Staric case studies from Czech Republic. *Eng. Geol.* **2012**, *147–148*, 37–51. [[CrossRef](#)]
17. Tao, T.; Liu, J.; Qu, X.; Gao, F. Real-time monitoring rapid ground subsidence using GNSS and Vondrak filter. *Acta Geophys.* **2018**, *67*, 133–140. [[CrossRef](#)]
18. Niethammer, U.; James, M.R.; Rothmund, S.; Travelletti, J.; Joswig, M. UAV-based remote sensing of the Super-Sauze landslide: Evaluation and results. *Eng. Geol.* **2012**, *128*, 2–11. [[CrossRef](#)]
19. Hu, S.; Qiu, H.; Pei, Y.; Cui, Y.; Xie, W.; Wang, X.; Yang, D.; Tu, X.; Zou, Q.; Cao, P.; et al. Digital terrain analysis of a landslide on the loess tableland using high-resolution topography data. *Landslides* **2018**, *16*, 617–632. [[CrossRef](#)]
20. Eker, R.; Aydın, A.; Hübl, J. Unmanned aerial vehicle (UAV)-based monitoring of a landslide: Gallenzerkogel landslide (Ybbs-Lower Austria) case study. *Environ. Monit. Assess.* **2018**, *190*, 28. [[CrossRef](#)]
21. Yang, D.; Qiu, H.; Hu, S.; Pei, Y.; Wang, X.; Du, C.; Long, Y.; Cao, M. Influence of successive landslides on topographic changes revealed by multitemporal high-resolution UAS-based DEM. *CATENA* **2021**, *202*, 105229. [[CrossRef](#)]
22. Ventura, G.; Vilaro, G.; Terranova, C.; Sessa, E.B. Tracking and evolution of complex active landslides by multi-temporal airborne LiDAR data: The Montaguto landslide (Southern Italy). *Remote Sens. Environ.* **2011**, *115*, 3237–3248. [[CrossRef](#)]
23. Li, Y.; Jiao, Q.; Hu, X.; Li, Z.; Li, B.; Zhang, J.; Ba, R. Detecting the slope movement after the 2018 Baige Landslides based on ground-based and space-borne radar observations. *Int. J. Appl. Earth Obs. Geoinf.* **2020**, *84*, 101949. [[CrossRef](#)]
24. Syzdykbayev, M.; Karimi, B.; Karimi, H. Persistent homology on LiDAR data to detect landslides. *Remote Sens. Environ.* **2020**, *246*, 111816. [[CrossRef](#)]
25. Schürch, P.; Densmore, A.L.; Rosser, N.J.; Lim, M.; McARDell, B.W. Detection of surface change in complex topography using terrestrial laser scanning: Application to the Illgraben debris-flow channel. *Earth Surf. Process. Landf.* **2011**, *36*, 1847–1859. [[CrossRef](#)]
26. Medjkane, M.; Maquaire, O.; Costa, S.; Roulland, T.; Letortu, P.; Fauchard, C.; Davidson, R. High-resolution monitoring of complex coastal morphology changes: Cross-efficiency of SfM and TLS-based survey (Vaches-Noires cliffs, Normandy, France). *Landslides* **2018**, *15*, 1097–1108. [[CrossRef](#)]
27. Stumvoll, M.; Schmaltz, E.; Glade, T. Dynamic characterization of a slow-moving landslide system—Assessing the challenges of small process scales utilizing multi-temporal TLS data. *Geomorphology* **2021**, *389*, 107803. [[CrossRef](#)]
28. Yang, D.; Qiu, H.; Hu, S.; Zhu, Y.; Cui, Y.; Du, C.; Liu, Z.; Pei, Y.; Cao, M. Spatiotemporal distribution and evolution characteristics of successive landslides on the Heifangtai tableland of the Chinese Loess Plateau. *Geomorphology* **2021**, *378*, 107619. [[CrossRef](#)]
29. Wasowski, J.; Bovenga, F. Investigating landslides and unstable slopes with satellite Multi Temporal Interferometry: Current issues and future perspectives. *Eng. Geol.* **2014**, *174*, 103–138. [[CrossRef](#)]
30. Bayer, B.; Simoni, A.; Schmidt, D.; Bertello, L. Using advanced InSAR techniques to monitor landslide deformations induced by tunneling in the Northern Apennines, Italy. *Eng. Geol.* **2017**, *226*, 20–32. [[CrossRef](#)]
31. Meng, Q.; Xu, Q.; Wang, B.; Li, W.; Peng, Y.; Peng, D.; Qi, X.; Zhou, D. Monitoring the regional deformation of loess landslides on the Heifangtai terrace using the Sentinel 1 time series interferometry technique. *Nat. Hazards* **2019**, *98*, 485–505. [[CrossRef](#)]
32. Berardino, P.; Fornaro, G.; Lanari, R.; Sansosti, E. A new algorithm for surface deformation monitoring based on small baseline differential SAR interferograms. *IEEE Trans. Geosci. Remote Sens.* **2002**, *40*, 2375–2383. [[CrossRef](#)]

33. Mora, O.; Lanari, R.; Mallorqui, J.J.; Berardino, P.; Sansosti, E. A new algorithm for monitoring localized deformation phenomena based on small baseline differential SAR interferograms. In Proceedings of the IEEE International Geoscience and Remote Sensing Symposium, Toronto, ON, Canada, 24–28 June 2002; pp. 1237–1239.
34. Ferretti, A.; Prati, C.; Rocca, F. Nonlinear subsidence rate estimation using permanent scatterers in differential SAR interferometry. *IEEE Trans. Geosci. Remote Sens.* **2000**, *38*, 2202–2212. [[CrossRef](#)]
35. Ferretti, A.; Prati, C.; Rocca, F. Permanent scatterers in SAR interferometry. *IEEE Trans. Geosci. Remote Sens.* **2001**, *39*, 8–20. [[CrossRef](#)]
36. Raucoules, D.; de Michele, M.; Malet, J.-P.; Ulrich, P. Time-variable 3D ground displacements from high-resolution synthetic aperture radar (SAR). Application to La Valette landslide (South French Alps). *Remote Sens. Environ.* **2013**, *139*, 198–204. [[CrossRef](#)]
37. Liu, X.; Zhao, C.; Zhang, Q.; Peng, J.; Zhu, W.; Lu, Z. Multi-Temporal Loess Landslide Inventory Mapping with C-, X- and L-Band SAR Datasets—A Case Study of Heifangtai Loess Landslides, China. *Remote Sens.* **2018**, *10*, 1756. [[CrossRef](#)]
38. Liu, X.; Zhao, C.; Zhang, Q.; Yang, C.; Zhu, W. Heifangtai loess landslide type and failure mode analysis with ascending and descending Spot-mode TerraSAR-X datasets. *Landslides* **2020**, *17*, 205–215. [[CrossRef](#)]
39. Highland, L.M.; Bobrowsky, P. The landslide handbook—A guide to understanding landslides: Reston, Virginia, U.S. *Geol. Surv. Circ.* **2008**, *1325*, 129.
40. Du, Y.; Xie, M.; Jia, J. Stepped settlement: A possible mechanism for translational landslides. *CATENA* **2019**, *187*, 104365. [[CrossRef](#)]
41. Bekaert, D.; Handwerger, A.; Agram, P.; Kirschbaum, D. InSAR-based detection method for mapping and monitoring slow-moving landslides in remote regions with steep and mountainous terrain: An application to Nepal. *Remote Sens. Environ.* **2020**, *249*, 111983. [[CrossRef](#)]
42. Ren, T.; Gong, W.; Gao, L.; Zhao, F.; Cheng, Z. An Interpretation Approach of Ascending–Descending SAR Data for Landslide Identification. *Remote Sens.* **2022**, *14*, 1299. [[CrossRef](#)]
43. Liu, Y.; Yang, H.; Wang, S.; Xu, L.; Peng, J. Monitoring and Stability Analysis of the Deformation in the Woda Landslide Area in Tibet, China by the DS-InSAR Method. *Remote Sens.* **2022**, *14*, 532. [[CrossRef](#)]
44. Zhang, Y.; Meng, X.; Dijkstra, T.; Jordan, C.; Chen, G.; Zeng, R.Q.; Novellino, A. Forecasting the magnitude of potential landslides based on InSAR techniques. *Remote Sens. Environ.* **2020**, *241*, 111738. [[CrossRef](#)]
45. Sun, Q.; Zhang, L.; Ding, X.; Hu, J.; Li, Z.; Zhu, J. Slope deformation prior to Zhouqu, China landslide from InSAR time series analysis. *Remote Sens. Environ.* **2014**, *156*, 45–57. [[CrossRef](#)]
46. Ma, S.; Qiu, H.; Hu, S.; Yang, D.; Liu, Z. Characteristics and geomorphology change detection analysis of the Jiangdingya landslide on July 12, 2018, China. *Landslides* **2021**, *18*, 383–396. [[CrossRef](#)]
47. Xie, M.; Zhao, W.; Ju, N.; He, C.; Huang, H.; Cui, Q. Landslide evolution assessment based on InSAR and real-time monitoring of a large reactivated landslide, Wenchuan, China. *Eng. Geol.* **2020**, *277*, 105781. [[CrossRef](#)]
48. Meng, Q.; Li, W.; Raspini, F.; Xu, Q.; Peng, Y.; Ju, Y.; Zheng, Y.; Casagli, N. Time-series analysis of the evolution of large-scale loess landslides using InSAR and UAV photogrammetry techniques: A case study in Hongheyan, Gansu Province, Northwest China. *Landslides* **2020**, *18*, 251–265. [[CrossRef](#)]
49. Xiong, Z.; Feng, G.; Feng, Z.; Miao, L.; Wang, Y.; Yang, D.; Luo, S. Pre- and post-failure spatial-temporal deformation pattern of the Baige landslide retrieved from multiple radar and optical satellite images. *Eng. Geol.* **2020**, *18*, 3475–3484. [[CrossRef](#)]
50. Squarzone, G.; Bayer, B.; Franceschini, S.; Simoni, A. Pre and post failure dynamics of landslides in the Northern Apennines revealed by space-borne synthetic aperture radar interferometry (InSAR). *Geomorphology* **2020**, *369*, 107353. [[CrossRef](#)]
51. Dai, K.; Xu, Q.; Li, Z.; Tomas, R.; Fan, X.; Dong, X.; Li, W.; Zhou, Z.; Gou, J.; Ran, P. Post-disaster assessment of 2017 catastrophic Xinmo landslide (China) by spaceborne SAR interferometry. *Landslides* **2020**, *16*, 1189–1199. [[CrossRef](#)]
52. Hou, R.; Chen, N.; Hu, G.; Han, Z.; Liu, E. Characteristics, mechanisms, and post-disaster lessons of the delayed semi-diagenetic landslide in Hanyuan, Sichuan, China. *Landslides* **2021**, *19*, 437–449. [[CrossRef](#)]
53. Li, M.; Zhang, L.; Dong, J.; Minggao, T.; Shi, X.; Liao, M.; Xu, Q. Characterization of pre- and post-failure displacements of the Huangnibazi landslide in Li County with multi-source satellite observations. *Eng. Geol.* **2019**, *257*, 105140. [[CrossRef](#)]
54. Zhu, Y.; Qiu, H.; Yang, D.; Liu, Z.; Ma, S.; Pei, Y.; He, J.; Du, C.; Sun, H. Pre- and post-failure spatiotemporal evolution of loess landslides: A case study of the Jiangou landslide in Ledu, China. *Landslides* **2021**, *18*, 3475–3484. [[CrossRef](#)]
55. Zhao, C.; Liu, X.; Zhang, Q.; Peng, J.; Xu, Q. Research on Loess Landslide Identification, Monitoring and Failure Mode with InSAR Technique in Heifangtai, Gansu. *Geomat. Inf. Sci. Wuhan Univ.* **2019**, *44*, 996–1007.
56. Wang, P. Regional landslide hazard assessment in Jianzha County, Qinghai Province based on logistic regression and GIS. *China Univ. Geosci.* **2017**.
57. Huang, R. Study on mechanism of typical rock landslide in western China. *Quat. Sci.* **2003**, *6*, 640–647.
58. Yin, Z.; Wei, G.; Qin, X.; Li, W.; Zhao, W. Research progress on landslides and dammed lakes in the upper Reaches of the Yellow River in the northeastern margin of the Tibetan Plateau. *Earth Sci. Front.* **2021**, *28*, 46–57.
59. Shi, L.; Wei, G.; Yin, Z.; Yuan, C.; Wu, X.; Li, Z. Development characteristics and genesis analysis of Simencun landslide in Jianzha Basin, Qinghai Province. *Chin. J. Geol. Hazard Control* **2020**, *31*, 15–21.
60. Strozzi, T.; Wegmuller, U.; Keusen, H.; Graf, K.; Wiesmann, A. Analysis of the Terrain Displacement Along a Funicular by SAR Interferometry. *Geosci. Remote Sens. Lett. IEEE* **2006**, *3*, 15–18. [[CrossRef](#)]

61. Werner, C.; Wegmuller, U.; Strozzi, T.; Wiesmann, A. Interferometric point target analysis for deformation mapping. IGARSS 2003. 2003 IEEE Int. Geosci. Remote Sens. Symp. **2003**, *7*, 4362–4364.
62. Graham, L.C. Synthetic interferometer radar for topographic mapping. *Proc. IEEE* **1974**, *62*, 763–768. [[CrossRef](#)]
63. Simons, M.; Rosen, P.A. Interferometric Synthetic Aperture Radar Geodesy. *Treatise Geophys.* **2007**, *3*, 391–446.
64. Ma, T.; Changjiang, L.; Lu, Z.; Wang, B. An effective antecedent precipitation model derived from the power-law relationship between landslide occurrence and rainfall level. *Geomorphology* **2014**, *216*, 187–192. [[CrossRef](#)]
65. Keefer, D.K.; Wilson, R.C.; Mark, R.K.; Brabb, E.E.; Brown, W.M., 3rd; Ellen, S.D.; Harp, E.L.; Wieczorek, G.F.; Alger, C.S.; Zarkin, R.S. Real-time landslide warning during heavy rainfall. *Science* **1987**, *238*, 921–925. [[CrossRef](#)]
66. Aleotti, P. A warning system for rainfall-induced shallow failures. *Eng. Geol.* **2004**, *73*, 247–265. [[CrossRef](#)]
67. Crozier, M.J.; Eyles, R.J. Assessing the probability of rapid mass movement. In Proceedings of the Third Australia-New Zealand conference on Geomechanics, Wellington, New Zealand, 12–16 May 1980; pp. 247–251.
68. Glade, T.; Crozier, M.; Smith, P. Applying Probability Determination to Refine Landslide-triggering Rainfall Thresholds Using an Empirical “Antecedent Daily Rainfall Model”. *Pure Appl. Geophys.* **2000**, *157*, 1059–1079. [[CrossRef](#)]
69. Yang, D.; Qiu, H.; Zhu, Y.; Liu, Z.; Pei, Y.; Ma, S.; Du, C.; Sun, H.; Liu, Y.; Cao, M. Landslide Characteristics and Evolution: What We Can Learn from Three Adjacent Landslides. *Remote Sens.* **2021**, *13*, 4579. [[CrossRef](#)]
70. Liu, Z.; Qiu, H.; Ma, S.; Yang, D.; Pei, Y.; Du, C.; Sun, H.; Hu, S.; Zhu, Y. Surface displacement and topographic change analysis of the Changhe landslide on September 14, 2019, China. *Landslides* **2021**, *18*, 1471–1483. [[CrossRef](#)]
71. Dong, J.; Zhang, L.; Tang, M.; Liao, M.; Xu, Q.; Gong, J.; Ao, M. Mapping landslide surface displacements with time series SAR interferometry by combining persistent and distributed scatterers: A case study of Jiaju landslide in Danba, China. *Remote Sens. Environ.* **2018**, *205*, 180–198. [[CrossRef](#)]
72. Larsen, I.; Montgomery, D. Landslide erosion coupled to tectonics and river incision. *Nat. Geosci.* **2012**, *5*, 468–473. [[CrossRef](#)]
73. Hu, X.; Wang, T.; Pierson, T.C.; Lu, Z.; Kim, J.; Cecere, T.H. Detecting seasonal landslide movement within the Cascade landslide complex (Washington) using time-series SAR imagery. *Remote Sens. Environ.* **2016**, *187*, 49–61. [[CrossRef](#)]
74. Liu, Y.; Qiu, H.; Yang, D.; Liu, Z.; Ma, S.; Pei, Y.; Zhang, J.; Tang, B. Deformation responses of landslides to seasonal rainfall based on InSAR and wavelet analysis. *Landslides* **2021**, *19*, 199–210. [[CrossRef](#)]
75. Cai, J.S.; Jim, Y.T.C.; Yan, E.C.; Tang, R.X.; Hao, Y.H.; Huang, S.Y.; Wen, J.C. Importance of variability in initial soil moisture and rainfalls on slope stability. *J. Hydrol.* **2019**, *571*, 265–278. [[CrossRef](#)]
76. Wu, W. Effect of seasonal frozen water on promoting slip—A new factor of landslide development. *J. Glaciol. Geocryol.* **1997**, *4*, 71–77.
77. Zhang, M.; Cheng, X.; Dong, Y.; Yu, G.; Zhu, L.; Pei, Y. Effect of frozen water and its slide-promoting mechanism: A case study of Heifang Tai area, Gansu Province. *Geol. Bull. China* **2013**, *32*, 852–860.
78. Ao, M.; Zhang, L.; Dong, Y.; Su, L.; Shi, X.; Balz, T.; Liao, M. Characterizing the evolution life cycle of the Sunkoshi landslide in Nepal with multi-source SAR data. *Sci. Rep.* **2020**, *10*, 17988. [[CrossRef](#)]
79. Guo, J.; Cui, Y.; Xu, W.; Yin, Y.; Li, Y.; Jin, W. Numerical investigation of the landslide-debris flow transformation process considering topographic and entrainment effects: A case study. *Landslides* **2022**, *19*, 773–788. [[CrossRef](#)]
80. Lei, M.; Cui, Y.; Ni, J.; Zhang, G.; Li, Y.; Wang, H.; Liu, D.; Yi, S.; Jin, W.; Zhou, L. Temporal evolution of the hydromechanical properties of soil-root systems in a forest fire in China. *Sci. Total Environ.* **2022**, *809*, 151165. [[CrossRef](#)]
81. Kuang, J.; Ng, A.H.-M.; Ge, L. Displacement Characterization and Spatial-Temporal Evolution of the 2020 Aniangzhai Landslide in Danba County Using Time-Series InSAR and Multi-Temporal Optical Dataset. *Remote Sens.* **2022**, *14*, 68. [[CrossRef](#)]
82. Jiao, Q.; Jiang, W.; Qian, H.; Li, Q. Research on characteristics and failure mechanism of Guizhou Shuicheng landslide based on InSAR and UAV data. *Nat. Hazards Res.* **2021**, *2*, 17–24. [[CrossRef](#)]